RESEARCH ARTICLE-MECHANICAL ENGINEERING

Simultaneous Influence of Hall and Wall Characteristics in Peristaltic Convective Carbon–Water Flow Subject to Soret and Dufour Effects

Zakir Hussain[1] · Taseer Muhammad[2]

Abstract

Peristalsis of carbon nanotubes (SWCNTs, MWCNTs) submerged in water through an inclined asymmetric channel is addressed in the current work. Such mechanism is disclosed in the presence of Hall effect, viscous dissipation, and Soret and Dufour effects. Convective heat transfer at the boundaries is incorporated by utilizing efficient thermal conductivity of nanoliquid. Low Reynolds number and long wavelength approximation are used for mathematical modeling. Resulting nonlinear set of equations is solved for pressure gradient, velocity, temperature and concentration. Impact of various variables on the axial velocity, pressure rise, pressure gradient, temperature, concentration, heat transport at boundaries and streamlines are discussed via their respective curves. Comparison between SWCNTs (single-wall carbon nanotubes) and MWCNTs (multiwall carbon nanotubes) is documented. Furthermore, submerging carbon nanotubes in water declines the velocity and temperature. In addition, heat transfer at the boundaries enhances by increasing volume fraction of carbon nanotubes. SWCNTs nanofluid shows higher velocity and concentration when compared with MWCNTs nanofluid. MWCNTs nanoliquid displays higher temperature than SWCNTs nanoliquid.

Keywords Peristalsis · Carbon nanotubes · Hall effect · Soret and Dufour effects · Convective conditions

List of symbols

Re	Reynolds variable
Fr	Froude variable
Br	Brinkman variable
Pr	Prandtl variable
Du	Dufour variable
Sc	Schmidt variable
Sr	Soret variable
B_0	Magnetic field
n	Number density of electrons
e	Electric charge
θ	Magnetic field inclination
m	Hall variable
μ_{nf}	Dynamic viscosity of nanofluid
μ_{f}	Dynamic viscosity of fluid
ϕ	Volume fraction of particle
ρ_{f}	The density of fluid
$(\rho c)_{\text{p}}$	Concrete heat storage of nanoparticles
$(\rho c)_{\text{f}}$	Heat storage of liquid
ρ_{nf}	Density of nanoliquid
ρ_{CNT}	Temperature and concentration of liquid
k_{f}	Thermal conductivity of base fluid
k_{CNT}	Nanotubes' thermal conductivity
$\bar{P}_{\star}$	The pressure
$C_{\star}$	The concentration
$T_{\star}$	The temperature
c_{p}	Specific heat at constant pressure
D	Mass diffusivity
K_{T}	Ratio of thermal diffusion
η_1	Coefficients of heat transport at top wall
η_2	Heat transfer coefficients at bottom wall
T_{a}	Ambient temperature
C_0	Concentration fields of the upper wall
C_1	Concentration fields of the lower wall
$d_1^{\star}, d_2^{\star}$	Ranges of top and bottom walls from center
$\bar{Y} = 0$	Centerline
$a_1^{\star}, a_2^{\star}$	Wave amplitudes at top and bottom walls
λ	Wavelength

✉ Zakir Hussain
zakir.qamar@yahoo.com; zakir.qamar@uobs.edu.pk

1 Department of Mathematics, University of Baltistan, Skardu 16100, Pakistan

2 Department of Mathematics, College of Sciences, King Khalid University, Abha 61413, Saudi Arabia

⚛ Springer

$\bar{t}_\star$	Time
ϕ_1	Phase variation range $0 \le \phi \le \pi$
$\rho_f g \sin \alpha$	Body force component along $\bar{X}$
$\rho_f g \cos \alpha$	Body force component along $\bar{Y}$
$\bar{H}_1^\star, \bar{H}_2^\star$	Bop and bottom walls of channel
$\bar{X}, \bar{Y}, \bar{t}_\star$	Laboratory frame
$h_1^{**}(x), h_2^{**}(x)$	Wall geometries
$\mathbf{V} = (\bar{U}_\star, \bar{V}_\star, 0)$	Velocity field
B_1 and B_2	Biot numbers at top and bottom walls of the channel

1 Introduction

Nanotechnology gained special attention of scientists from the area of mote biology, superficial science, physics, chemistry and mote engineering. However, commercialization of nanotechnology utilizes nano-sized (10^9) particle in bulk. One such industry is to produce nanofluids by infusing metal or ceramic nanoparticles in a base fluid. Mini size of such nanoparticles optimizes the surface area coverage while economizing it commercially. Even nanoparticles have special significance in tissue engineering. Recently, scientists have manufactured DNA origami-based nanobots that are able to lead out logic functions to gain pinned drug supply for cancer-affected people. Metal particles in nanofluids allow more rapid change in thermal status compared to general fluids. Such effectiveness of nanofluids is crucial for coolants in nuclear reactor and computer processors. Chemical industries utilize nanofluids in the production of catalysts. Few recent studies regarding flows of nanofluids can be observed via Refs. [1–13].

Processes like hemodialysis, transportation of corrosive fluids, movement of insects and food bolus in esophagus are because of peristaltic motion. Peristalsis is a unique pattern of smooth muscular contractions that propels biological fluids through the esophagus and intestines in human body. Nuclear industries utilize peristaltic activity during transportation of highly explosive and corrosive materials. In biomedical field, contamination in biological fluids during dialysis and open heart surgeries is avoided by utilizing peristaltic transport via finger and roller pumps. Previous studies on peristaltic function were suggested by Shapiro et al. [14] and Latham [15]. Infusing nanoparticles with peristalsis has novel significance in biomedical engineering as it improves solubility and conducts heat energy more efficiently. Medically, organic antibacterial drugs at high temperatures are not stable; however, drugs including metals and metal oxides, due to their high thermal conductivity, are much more suitable. Hence, the use of nanoparticles in cancer drugs not only enhances their therapeutic significance but also by using externally applied magnetic field. Drug can be navigated to the required cancerous site. Such significance of nanofluids in peristaltic

activities motivated the scientists to further explore this topic [16–32].

Investigation of peristaltic transport under influence of magnetic field becomes more significant with reference to electrified liquid like blood, salt liquid, fluid metals and plasma. Magnetohydrodynamics (MHD) has many practical applications in diagnosis of diseases, control of cooling process during many manufacturing processes, nuclear plants, cure inflammation, solidification of metals, gas turbines, radar system and many more. Hall currents are generated by magnetic field which affect the current density of fluid. The processes including weak magnetic forces and Hall effect can be neglected. However, for powerful magnetic forces, the Hall effect becomes significant and strongly influences the current density during hydromagnetic heat transfer. Modification of Ohm's law is required in mathematical modeling of such processes. Analysis of impact of magnetic field with Hall currents on movement of blood via arteries is valuable in order to understand magnetic resonance angiography (MRA) that is employed to visualize arteries for diagnosis of stenosis and many other abnormalities. Few applications of Hall effect along with heat transfer include power generation, electric transformer, MHD accelerators, nanotechnological processing, heating elements and Hall accelerators. Few remarkable attempts on analysis of the above effects on peristalsis can be cited through Refs. [33–40].

Peristaltic movement with transportation of heat and mass is widely used in the biomedical field. Oxygenation and hemodialysis processes can be observed by using peristalsis with heat transfer. Heat transfer occurring in biological tissues is involved in heat convection caused by blood flow in tissue pores, heat conduction in tissues, food processing and vasodilation and radiative transfer of heat between surface and environment. Mass transfer phenomenon is also present in organisms. Mass transfer also has many applications in industry. It is used in many processes such as reverse osmosis, combustion process and distillation process. The phenomenon containing combined transfer of heat and mass, the simultaneous density difference is produced by concentration gradient, material composition and temperature gradient. Soret–Dufour effect is used in various processes of physics and engineering, such as geothermal system drying technology, chemical engineering, heat insulation, geoscience and chemical engineering. Dufour effect deals with energy flux produced by concentration gradient. A change in temperature because of mass flux is termed as Soret effect. Soret effect is extensively used for separation of isotopes. Influence of Soret and Dufour effects is sometime neglected because of their small magnitudes. However, in some cases they cannot be neglected such as in geosciences. These effects are of great importance due to their significance in the study of fluids with low and medium molecular weight.

Some investigations focusing on impact of Soret and Dufour effects are reported in the literature (see Ref. [41–51]).

The current study has novelty in computation, modeling and associated analysis through comparison. The analysis gives a comparative study of CNTs nanoliquids. Explicitly, the purpose of this work is to disclose the analysis in five dimensions: first, to formulate the problem; second, to investigate Hall effect in nanoliquid flow; third, to examine the convective heat transfer at the boundaries accounts for the bulk movement of nanoliquid. It is necessary to consider convective conditions at the boundaries to examine the heat transport in peristalsis nanoliquids accurately; fourth, comparison of SWCNTs and MWCNTs nanoliquids that treat water as a base liquid; and fifth Soret and Dufour effects are also incorporated in nanoliquid flow for heat and mass transfer analysis. The investigation is carried out in an inclined asymmetric channel. Mathematical formulation is simplified subject to low Reynolds number and long wavelength. The graphical results are presented for flow, temperature, pressure gradient, concentration and trapping for various parameters.

2 Formulation

Consider peristaltic convective flow of incompressible carbon–water nanoliquid in asymmetric channel of thickness $d_1^\star$ and $d_2^\star$. The sinusoidal wave (λ) with wave speed (c) that grows along the channel causes the peristalsis of carbon–water liquid. X-axis is taken along the channel, while Y-axis is normal to it in Cartesian coordinate. The channel is fixed at an angle α. Water is treated as a base liquid, and CNTs (SWCNT, MWCNT) are nanoparticles that submerge in the base liquid. Inclined magnetic field develops electricity in base liquid. Furthermore, Hall effects are also incorporated for flow analysis. Heat and mass transfers are analyzed via influence of Soret and Dufour effects. Convective conditions confirm the walls channel. The magnetic field is eliminated for small Reynolds number. Figure 1 addresses the geometry of problem. Laboratory frame is dealt via xy-plane (Table 1).

Following Xue [52]

$$
\begin{cases}
\mu_{nf} = \dfrac{\mu_f}{(1-\phi)^{2.5}}, \quad \nu_{nf} = \dfrac{\mu_{nf}}{\rho_{nf}}, \quad \rho_{nf} = (1-\phi)\,\rho_f + \phi\rho_{CNT}, \\[2mm]
\alpha_{nf} = \dfrac{k_{nf}}{\rho_{nf}(c_p)_{nf}}, \quad G_1 = \dfrac{k_{nf}}{k_f} = \dfrac{(1-\phi)+2\phi\frac{k_{CNT}}{k_{CNT}-k_f}\ln\frac{k_{CNT}+k_f}{2k_f}}{(1-\phi)+2\phi\frac{k_f}{k_{CNT}-k_f}\ln\frac{k_{CNT}+k_f}{2k_f}}, \\[3mm]
\dfrac{\sigma_{nf}}{\sigma_f} = \left(\dfrac{3(\sigma^*-1)\phi}{(\sigma^*+2)-(\sigma^*-1)\phi}+1\right).
\end{cases}
\tag{1}
$$

The long wavelength and low Reynolds number (Re $\to$ 0) assumptions are as follows:

$$
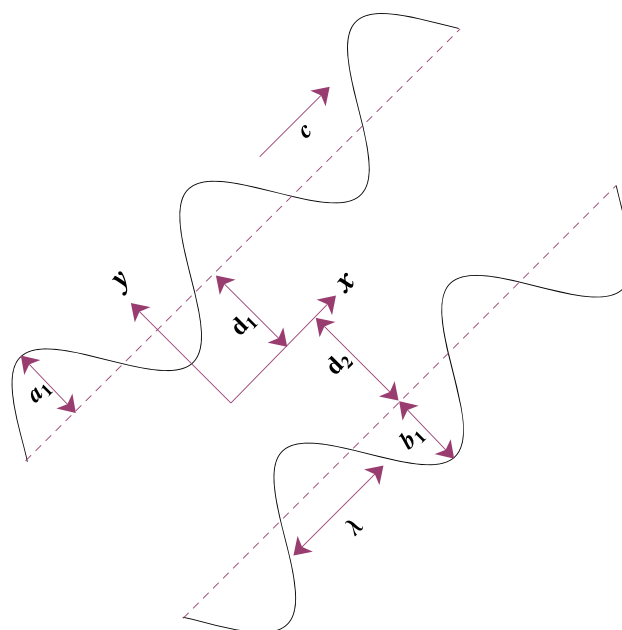-\frac{dp_\star}{dx} + \frac{1}{(1+\phi)^{2.5}}\frac{\partial^2 u_\star}{\partial y^2} - \frac{M^2}{1+m^2}
$$

Fig. 1 Schematic representation of problem

Table 1 Thermophysical features of CNTs (SWCNT, MWCNT) [53]

Physical features	Base liquid	Nanoparticles	
	Water	SWCNTs	MWCNTs
ρ (kg/m^3)	997	2600	1600
c_p (J/kg K)	4179	425	796
k (W/mK)	0.613	6600	3000
σ^* (S/m)	0.005	–	–

$$
\cos\theta\left(\frac{3(\sigma^*-1)\phi}{(\sigma^*+2)+(\sigma^*-1)\phi}+1\right)(u_\star\cos\theta+\cos\theta)
$$
$$
+\left(1+\phi+\frac{\phi_{CNT}}{\rho_f}\right)\frac{Re}{Fr}\sin\alpha = 0,
\tag{2}
$$

$$
-\frac{\partial p_\star}{\partial y} = 0,
\tag{3}
$$

$$
G_1\frac{\partial^2\gamma}{\partial y^2} + Br\frac{1}{(1-\phi)^{2.5}}\left(\frac{\partial u_\star}{\partial y}\right)^2
$$
$$
+ \Pr Du\left(1+\phi+\frac{\phi_{CNT}}{\rho_f}\right)\frac{\partial^2\varphi}{\partial y^2} = 0,
\tag{4}
$$

$$
\frac{\partial^2\varphi}{\partial y^2} + ScSr\frac{\partial^2\gamma}{\partial y^2} = 0.
\tag{5}
$$

The dimensionless forms of boundary conditions are

$$
u_\star = -1, \quad G_1\frac{\partial\gamma}{\partial y} + B_1\gamma = 0, \quad \varphi = 0,
$$
$$
\text{at} \quad y = h_1^{**\star}(x) = 1 + a_1\sin(2\pi x),
$$

$$u_\star = -1, \quad G_2\frac{\partial\gamma}{\partial y} - B_2\gamma = 0, \quad \varphi = 1,$$

$$\text{at} \quad y = h_2^{**}(x) = -d_1^\star - b_1^\star \sin(2\pi x + \phi_1). \tag{6}$$

The condition satisfies via $a_1 = a_1^*/d_1^*$, $b_1^* = a_2^*/d_1^*$ and $d_1^{**} = d_2^*/d_1^*$,

$$a_1^2 + b_1^{\star 2} + 2a_1 b_1^\star \cos\phi_1 \le (1 + d_1^{\star\star})^2. \tag{7}$$

In wave frame, average flux F is described by

$$F = \int_{h_2^{\star*}}^{h_1^{\star*}} u\,dy. \tag{8}$$

The relation between average flux in wave (F) and laboratory (σ) frames is stated as

$$\sigma = F + 1 + d_1^{\star\star}. \tag{9}$$

The pressure rise per wavelength (Δp_λ) in non-dimensional form is

$$\Delta p_\lambda = \int_0^1 \left(\frac{dp_\star}{dx}\right) dx. \tag{10}$$

Develop the following dimensionless quantities utilized in the above equations (see "Appendix" for more details):

$$x = \frac{\bar{x}}{\lambda}, \quad y = \frac{\bar{y}}{d_1^\star}, \quad u = \frac{\bar{u}_\star}{c}, \quad v = \frac{\bar{v}_\star}{c\delta}, \quad p = \frac{d_1^{\star 2}}{c\mu_f\lambda}\bar{p}_\star,$$

$$h_1^\star = \frac{\bar{h}_1^\star}{d_1}, \quad h_2^\star = \frac{\bar{h}_2^\star}{d_1^\star}, \quad \delta = \frac{d_1^\star}{\lambda},$$

$$\text{Fr} = \frac{c^2}{gd_1^\star}, \quad \kappa = \frac{k_0 c}{\mu_f d_1^\star}, \quad \gamma = \frac{T_\star - T_a}{T_a}, \quad \text{Ec} = \frac{c^2}{c_p T_a},$$

$$\text{Pr} = \frac{c_p\mu_f}{k_f}, \quad \varphi = \frac{C_\star - C_0}{C_1 - C_0}, \quad \text{Sc} = \frac{\mu_f}{\rho_f D},$$

$$\text{Sr} = \frac{\rho_f D K_T T_a}{\mu_f T_m (C_1 - C_0)}, \quad M^2 = \frac{\sigma_f B_0^2 d_1^{\star 2}}{\mu_f},$$

$$\text{Br} = \text{Pr Ec}, \quad B_1 = \frac{\eta_1 d_1^\star}{\kappa_f}, \quad B_2 = \frac{\eta_2 d_1^\star}{\kappa_f},$$

$$\text{Du} = \frac{\rho_f D K_T (C_1 - C_0)}{\mu_f c_p c_s T_a}, \quad m = \sigma^* B_0/en, \quad \text{Re} = \frac{\rho_f c d_1^\star}{\mu_f}. \tag{11}$$

3 Discussion

This portion focuses on the graphical outcome of different pertinent variables for velocity, temperature, concentration, pressure gradient and pressure rise.
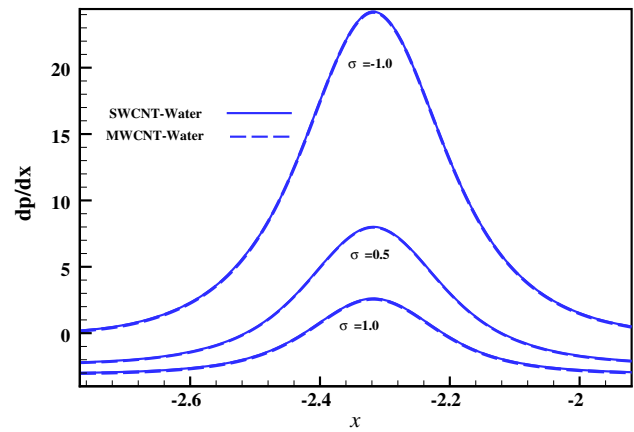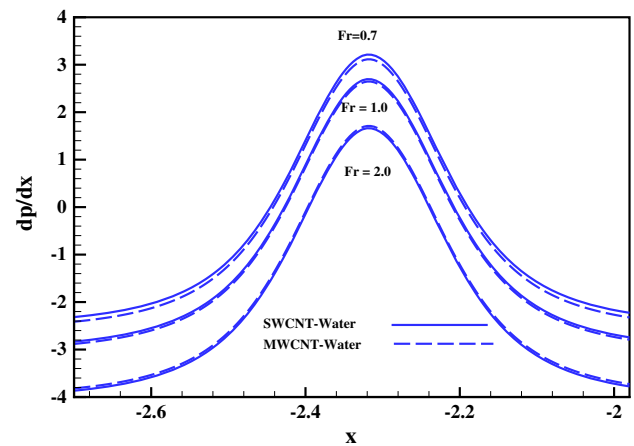
Fig. 2 Plots for pressure gradient via σ

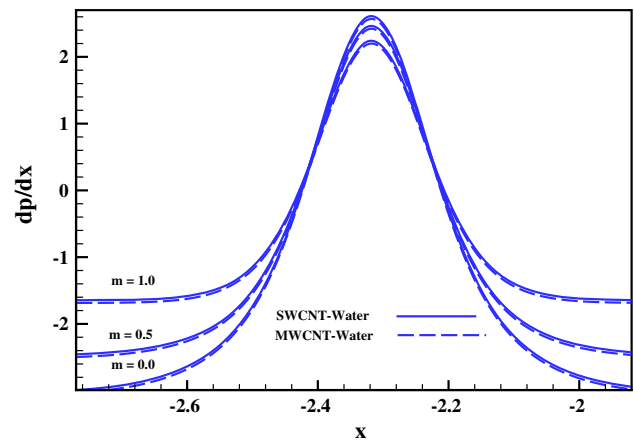**Fig. 3** Plots for pressure gradient via Fr

Fig. 4 Plots for pressure gradient via m

3.1 Pressure gradient analysis

Oscillatory trend for pressure gradient is noticed because of peristalsis from Figs. 2, 3, 4, 5, 6, 7 and 8. The values of these parameters ($a_1 = 0.7, b_1^* = 0.4, d_1^* = 0.5, \phi =$
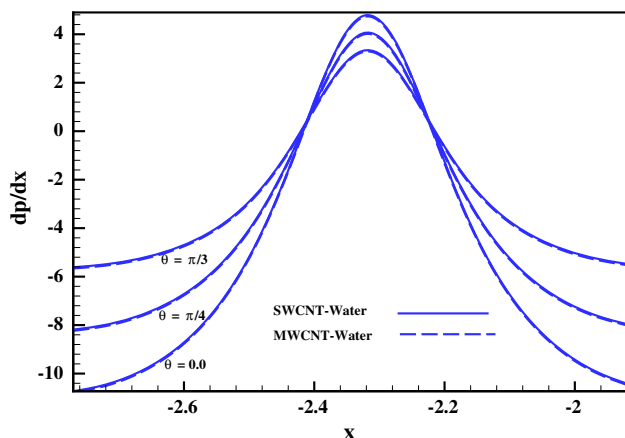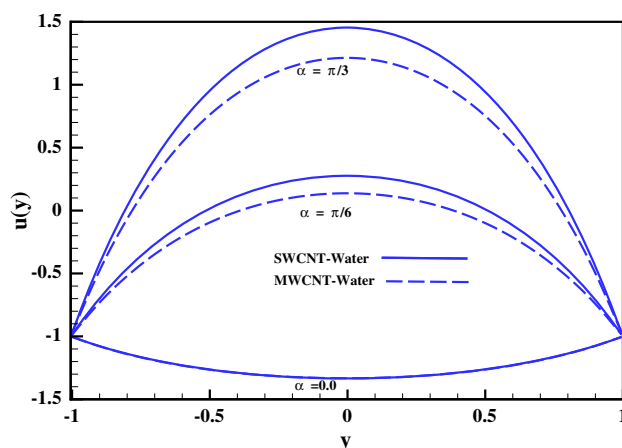
Fig. 5 Plots for pressure gradient via θ
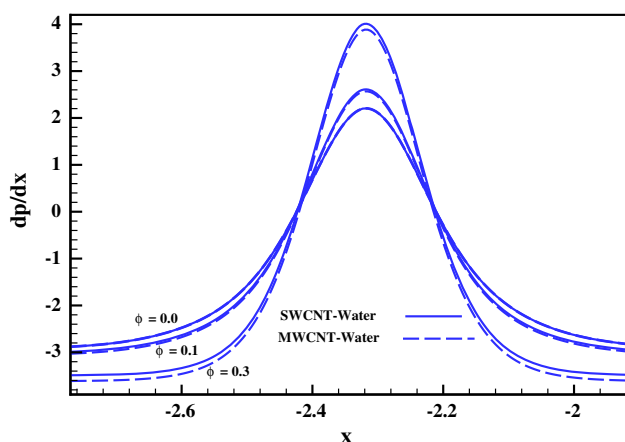

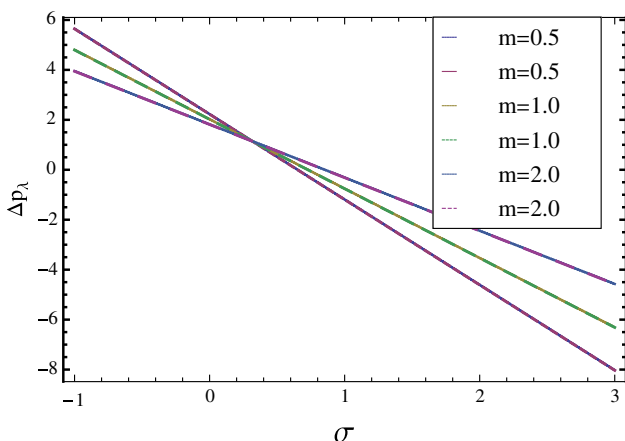**Fig. 6** Plots for pressure gradient via ϕ

Fig. 7 Plots for pressure rise via m

0.01, Fr = 1.4, σ = 1.2, $\alpha = \frac{\pi}{4}$, $\phi_1 = \frac{\pi}{3}$, m = 0.04, M = 3, $\theta = \frac{\pi}{6}$, Du = 0.3, B_1 = 8.0, B_2 = 8.0, Sc = 0.7, Sr = 0.7, Pr = 6.2, Br = 3.0) dealt unchanged except the variable in figure. Figures 2, 2, 3, 4, 5, 6, 7 and 8 discuss features of σ, Fr, m, θ and ϕ for pressure change $\left(\frac{dp_\star}{dx}\right)$

Fig. 8 Plots for pressure rise via θ

and pressure rise (Δp_λ). These figures disclosed that $\frac{dp_\star}{dx}$ is an oscillating function over the length of walls. Figure 2 shows that the pressure declines for the incremented values of σ (average flux) against SWCNT liquid and MWCNT liquid. The pressure gradient for SWCNTs liquid is noted higher than MWCNTs liquid. Figure 3 addresses that the pressure decays rapidly in MWCNT liquid than SWCNT liquid for increasing values of Froude number. Moreover, larger Fr declines the pressure gradient for both nanoliquids. Because the gravitational effects are weakened when Froude number increased, the resulting average pressure rise declines. The behavior of pressure gradient is shown in Fig. 4 for Hall number (m). The pressure gradient at the center of channel declines, and it enhances close to the boundary wall as the values of m increase. The pressure in case of SWCNTs nanoliquid is observed maximum when compared with MWCNTs nanoliquid against higher values of m. Figure 5 shows increasing behavior of pressure change near the wall channel, and it decreases at the center of channel for higher values of inclination angle. The behavior of volume fraction of nanoparticles against pressure gradient is shown in Fig. 6. Figure 6 addresses the oscillatory trend for the pressure gradient via peristalsis. The pressure gradient reaches the highest value near the center part of the channel during one complete oscillation. It decreases near the wider part of channel with addition of nanotubes volume fractions. SWCNTs water is prominent than MWCNTs water. The pressure rise enhances in ($\Delta p_\lambda < 0, \sigma > 0$) (co-pumping region), and it decreases in ($\Delta p_\lambda > 0, \sigma < 0$) (retrograde region) for larger Hall variable m. Figure 8 reveals that pressure rise accelerates in ($\Delta p_\lambda < 0, \sigma > 0$) (co-pumping region), and it declines in ($\Delta p_\lambda > 0, \sigma > 0$) (peristaltic pumping region) as magnetic inclination angle (θ) increases. Similar trend is noted for both SWCNTs and MWCNTs nanoliquids.
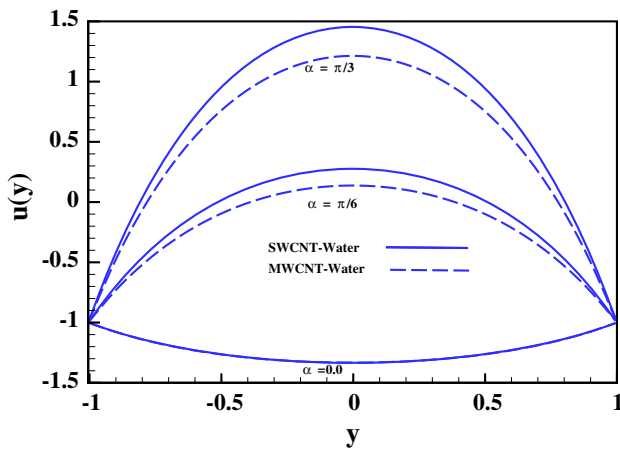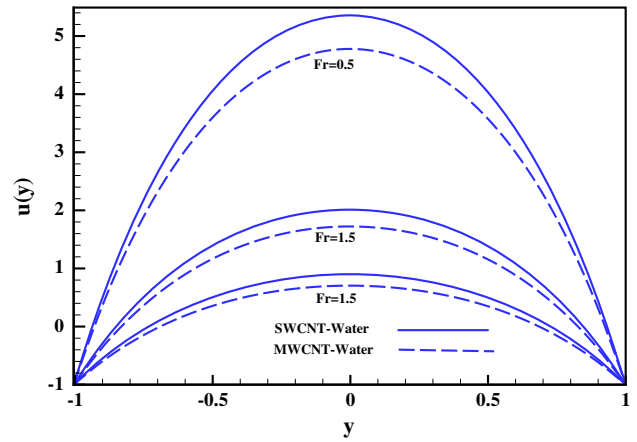
Fig. 9 Plots for velocity via α
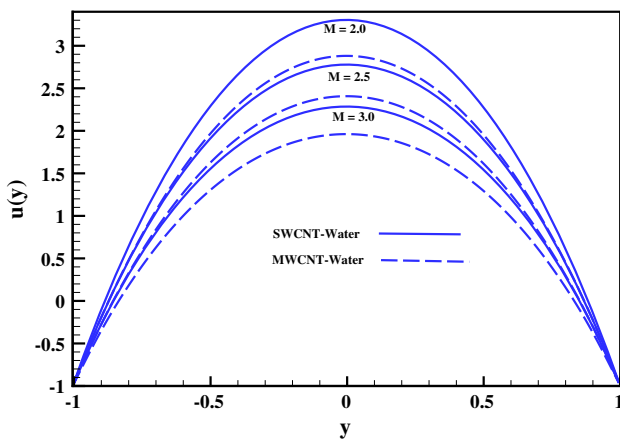

Fig. 10 Plots for velocity via M

Fig. 11 Plots for velocity via m

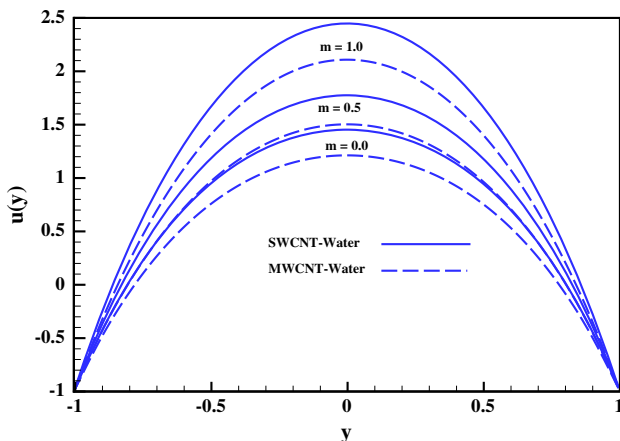

Fig. 12 Plots for velocity via Fr

Fig. 13 Plots for velocity via θ
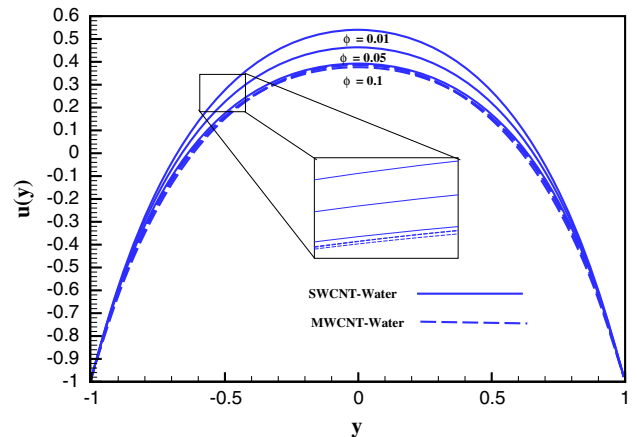

Fig. 14 Plots for velocity via ϕ

3.2 Flow behavior analysis

It is followed from Figs. 9, 10, 11, 12, 13 and 14 that the velocity profile leads to a parabolic path having maximum output near the center of channel. The values of these parameters

$(a_1 = 0.7, b_1^* = 0.4, d_1^* = 0.5, \phi = 0.01, \text{Fr} = 1.4, \sigma = 1.2, \alpha = \frac{\pi}{4}, \phi_1 = \frac{\pi}{3}, m = 0.04, M = 3, \theta = \frac{\pi}{6}, x = -0.5, \frac{dp}{dx} = 1.2, \text{Du} = 0.3, B_1 = 8.0, B_2 = 8.0, \text{Sc} = 0.7, \text{Sr} = 0.7, \text{Pr} = 6.2, \text{Br} = 3.0)$ remained fixed except the variable defined in figure. Figures 9, 10, 11, 12, 13 and 14
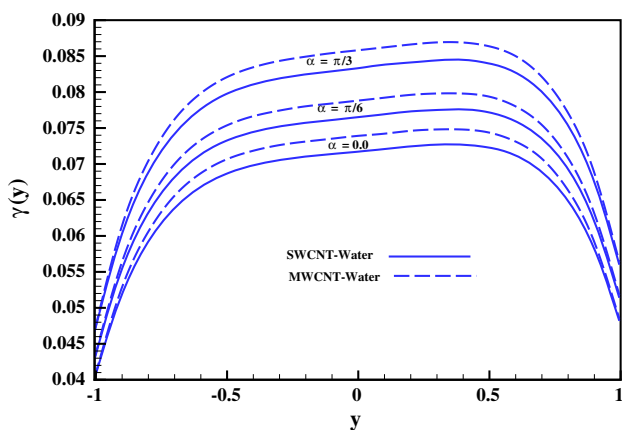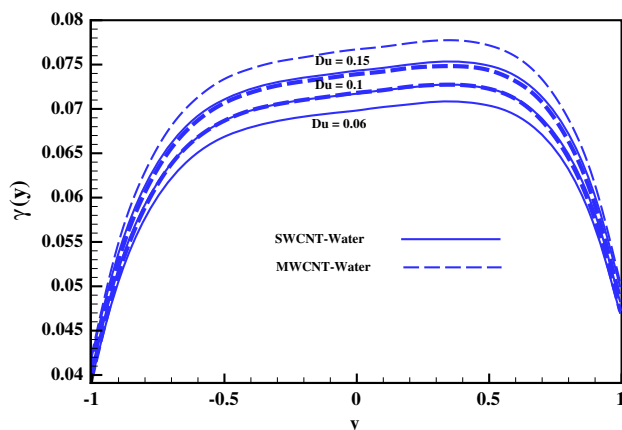
Fig. 15 Plots for temperature via α

Fig. 16 Plots for temperature via B_1
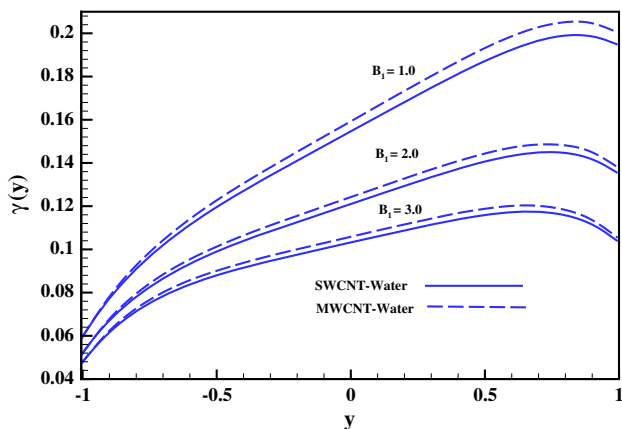

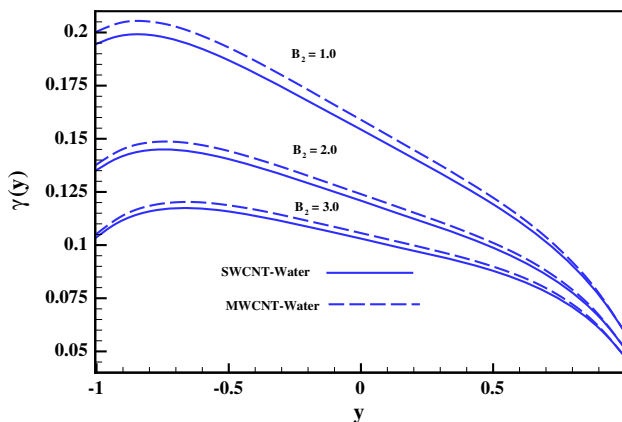**Fig. 17** Plots for temperature via B_2

Fig. 18 Plots for temperature via B_r

demonstrate the fluctuations in velocity distribution with a change in inclination of channel α, Hartmann number (M), Hall variable (m), Froude number (Fr), inclination of magnetic field (α) and volume fraction variable (ϕ). The velocity is maximized with an increment in α depicted in Fig. 9. It is observed from the figure that large inclination angle corre-

sponds to maximum velocity. Physically higher inclination angle tends to enhance the impact of gravity, resulting in an increase in the velocity. The velocity of water base liquid is noted higher for SWCNTs than MWCNTs. Hartmann number (M) outcomes can be observed via Fig. 10. Larger M tends to decline the velocity. Higher Hartmann number leads to Lorentz force that resists the liquid flow, resulting in decreases in the velocity. The velocity is noted higher at the center of channel for SWCNTs when compared with MWC-NTs. The behavior of velocity against Hall parameter m is shown in Fig. 11. The figure depicts that higher values of m correspond to maximum velocity in the middle of the channel. Furthermore, the velocity in case of SWCNTs is noted higher than MWCNTs. Figure 12 is plotted against Fr. Larger Fr corresponds to decline in the velocity at the center of channel. It is due to the fact that higher values of Fr tend to weak gravitational force in the inclined channel, and consequently it declines the velocity of nanoliquid. Velocity for SWCNTs water is prominent than MWCNTs water. Effect of higher inclination angle of magnetic field is demonstrated in Fig. 13. The longitudinal velocity (u) is higher when compared with $\theta = 0$. The higher inclination angle helps to boost the velocity of nanoliquid. Furthermore, the larger magnetic tendency increases the velocity of nanoliquid because magnetic field inclines at greater angle and the effect of magnetic field is reversed on liquid particles. In addition to, in turn declines the influence resulting liquid velocity is up graded. SWNTs water boosts the velocity when compared with MWCNTs water. From Fig. 14, decrement in u is noticed for larger ϕ. Submerging of CNTs in base liquid declines the maximum velocity of fluid, because the submerging of nanotubes in base liquid enhances the effective viscosity of liquid. The velocity for SWCNT liquid is noted greater compared to MWCNT liquid.
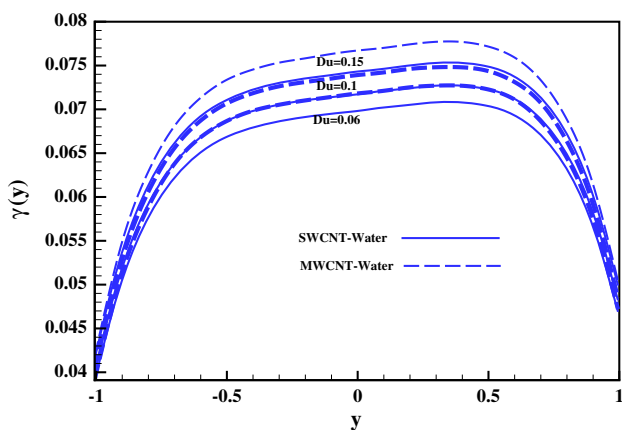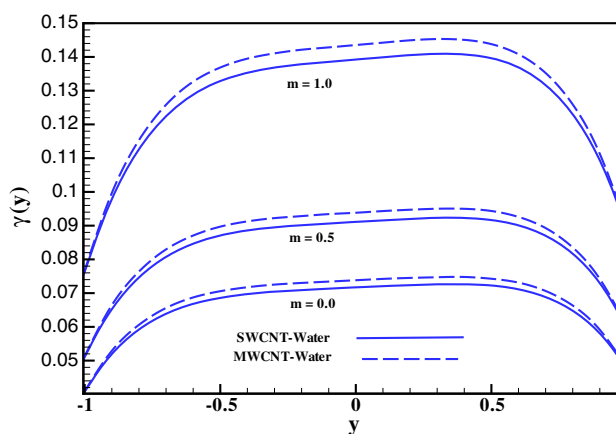
Fig. 19 Plots for temperature via Du
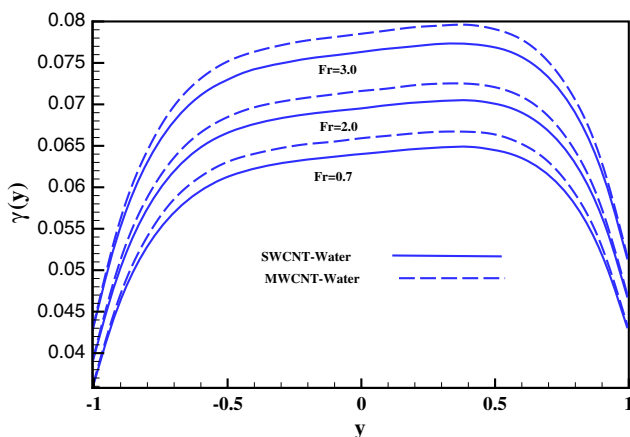

Fig. 20 Plots for temperature via Fr

Fig. 21 Plots for temperature via M

Fig. 22 Plots for temperature via m
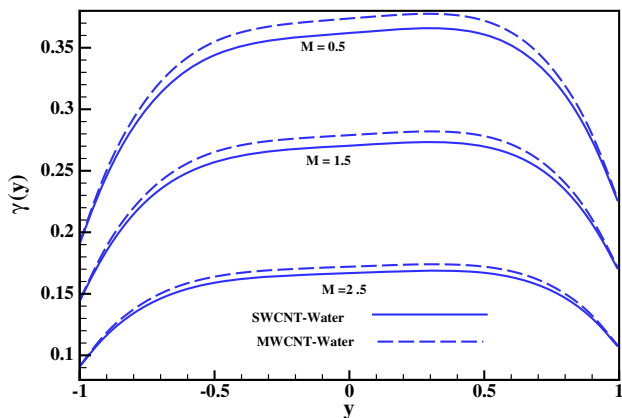
Fig. 23 Plots for temperature via θ
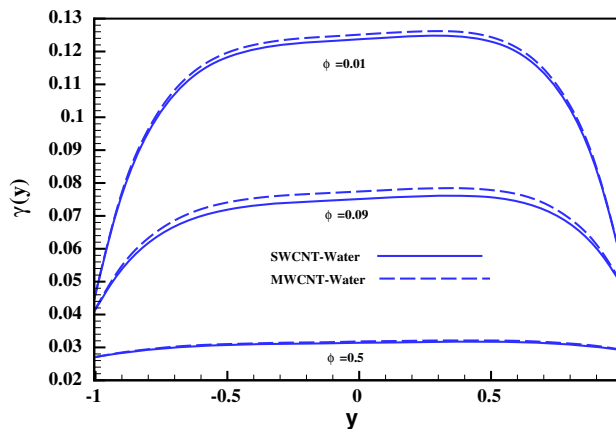
Fig. 24 Plots for temperature via ϕ

3.3 Temperature analysis

It is seen from graphical results (see Figs. 15, 16, 17, 18, 19, 20, 21, 22, 23) that temperature curves attain maximum value at the center of the channel. The values of these parameters ($a_1 = 0.7$, $b_1^* = 0.4$, $d_1^* = 0.5$, $\phi = 0.01$, Fr $= 1.4$, $\sigma =$

1.2, $\alpha = \frac{\pi}{4}$, $\phi_1 = \frac{\pi}{3}$, $m = 0.04$, $M = 3$, $\theta = \frac{\pi}{6}$, $x = -0.5$, $\frac{\mathrm{d}p}{\mathrm{d}x} = 1.2$, Du $= 0.3$, $B_1 = 8.0$, $B_2 = 8.0$, Sc $= 0.7$, Sr $= 0.7$, Pr $= 6.2$, Br $= 3.0$) were treated constant except the variable dealt in the figure. The effect of temperature (γ) for different pertinent parameters can be seen via Figs. 15, 16, 17, 18, 19, 20, 21, 22 and 23. Fig-

Fig. 25 Plots for concentration via Sc

ure 15 reveals that temperature increases for growing values of magnetic inclination parameter (α). In fact, increasing velocity due to inclination causes an increase in viscous dissipation. The resulting temperature of nanoliquid enhances. Temperature in the case of MWCNTs 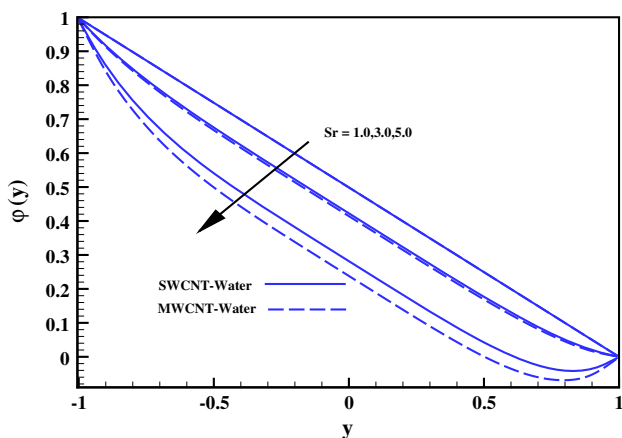is noted higher than SWCNTs. The impact of heat Biot number on temperature is portrayed in Fig. 16. In fact, the process of heat mechanism is accelerated for greater Biot variable and consequently temperature decays. Here, it is considered larger Biot number and a nonuniform temperature field is noticed within the liquid. Furthermore, convective boundary conditions provide the heat transport through the liquid–solid interface. The temperature decreases for higher values of B_2 (Fig. 17). Temperature in case of MWCNTs is noted higher when compared with SWCNTs. Figure 18 shows the effect of Brinkman number (Br) against temperature profile γ. It is noticed that for Br = 0.0 there is no effect of viscous dissipation. Higher values of Br correspond to an increase in the temperature of nanoliquid due to addition of viscous dissipation effect. Physically, internal resistance of particles in fluid increases which enhances the temperature for larger Br and so γ increases. Figures 19 and 20 show increasing behavior of temperature curves for larger values of Du and Fr. In addition, for greater values of M and m, the temperatures of electrified nanoliquid decrease (see Figs. 21, 22). It is due to the fact that kinetic energy of electrified liquid molecules is directly related to temperature that shows a reduction in temperature for larger M and m. The temperature for MWCNTs nanoliquid is noted higher when compared with SWCNTs nanoliquid. Figure 23 addresses the curves for temperature against higher values of inclination angle. It is seen from the figure that larger θ results in an increase in the temperature. The behavior of nanoparticles volume fraction is reported in Fig. 24. The temperature of nanoliquid declines close to the center of channel when volume fraction of nanotubes is enhanced. In fact, increasing the nanoparticles volume fraction enhances the thermal

conductivity of nanoliquid and consequently the temperature of nanoliquid declines. The temperature of MWCNTs nanoliquid decreases rapidly when compared with SWCNTs nanoliquid temperature.

3.4 Concentration analysis

Impact of some occurring physical parameters on concentration distribution is sketched through Figs. 24 and 25. The values of these variables ($a_1 = 0.7$, $b_1^* = 0.4$, $d_1^* = 0.5$, $\phi = 0.01$, Fr = 1.4, $\sigma = 1.2$, $\alpha = \frac{\pi}{4}$, $\phi_1 = \frac{\pi}{3}$, $m = 0.04$, $M = 3$, $\theta = \frac{\pi}{6}$, $x = -0.5$, $\frac{dp}{dx} = 1.2$, Du = 0.3, $B_1 = 8.0$, $B_2 = 8.0$, Sc = 0.7, Sr = 0.7, Pr = 6.2, Br = 3.0) remained constant except the parameter in the figure. In Fig. 25, concentration profile shows a decreasing impact via larger Sc. Since fluid density decreases due to a decrease in momentum of nanoliquid and mass diffusion phenomena for larger Sc, the concentration declines. The concentration profile declines for larger Sr (see Fig. 26). This is due to the fact that larger Soret number boosts mass flux which results in decay in concentration. The concentration for SWCNTs nanoliquid is observed higher when compared with MWCNTs nanoliquid.

Phenomena of trapping for sundry physical parameters, namely ϕ, m, M and ϕ_1, for both SWCNT and MWCNT are sketched in Figs. 27, 28, 29, 30 and 31. Trapping occurs when some streamlines split and form circulating bolus under certain conditions. The size of bolus increases for increasing inclination parameter for both cases (see Fig. 27). The size of bolus in MWCNTs water is noted similar to SWCNTs water. In Fig. 28, it is noticed that for larger m, the size of trapped bolus rapidly declines for both SWCNT and MWCNT. The same behavior is observed for both types of nanotubes. The larger values of Hartmann number (M) result in an increase in the bolus size (see Fig. 29). SWCNTs and MWCNTs both show the same behavior for larger M. For greater values of volume fraction (ϕ), the bolus disappears for SWCNTs, whereas the size of bolus grows minutely for MWCNT (see Fig. 30). For larger ϕ_1, the bolus vanishes for SWCNT, whereas for MWCNT, the bolus size becomes large (see Fig. 31) as the values of ϕ_1 increase.

4 Conclusion

Impact of carbon nanotubes (CNTs) on the peristaltic transport via an inclined asymmetric channel is reported. Hall number, viscous dissipation, and Soret and Dufour effects are considered. Contribution of different parameters on velocity, pressure gradient, temperature, concentration and heat transfer is analyzed. Convective movement of peristaltic carbon–water liquid via inclined asymmetric walls has been

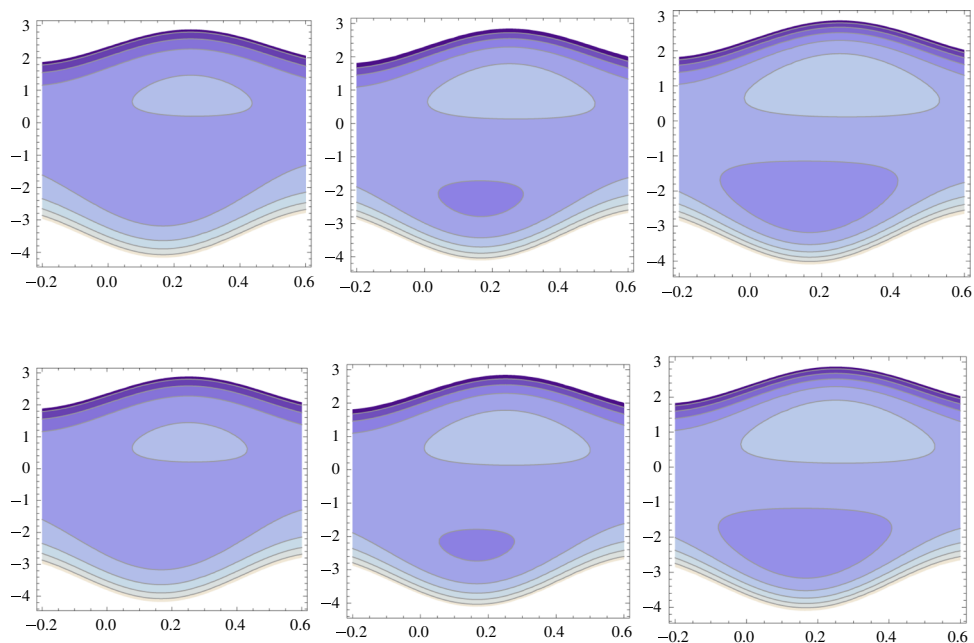**Fig. 26** Plots for concentration via Sr

Fig. 27 Streamlines in case of SWCNTs and MWCNTs via $\alpha = \frac{\pi}{4}, \alpha = \frac{\pi}{3}, \alpha = \frac{\pi}{2}$
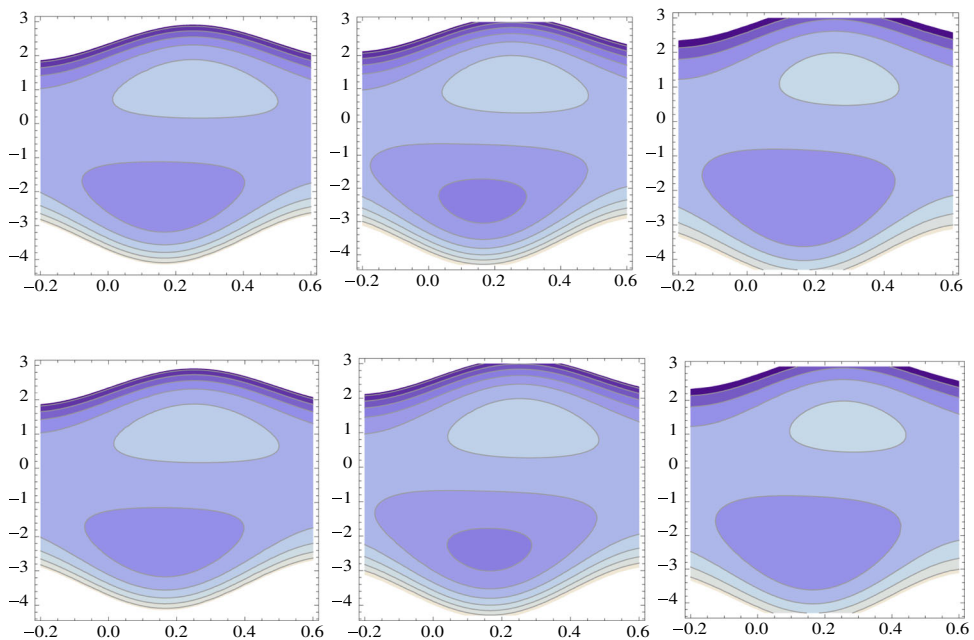
discussed in the current study. Hall effect is incorporated to study the movement of CNTs-submerged liquid. Heat and mass transport analysis has been pictured via Soret and Dufour effects. The key findings of the current study are listed as follows:

- Addition of SWCNTs and MWCNTs in base liquid decline the fluid velocity close to the center of the channel because of the resistance providing to the fluid motion.

- Enhancement in SWCNTs and MWCNTs volume fractions increases the rate of heat transfer at the boundary and declines the temperature at center of the channel.
- Addition of CNTs enhances the pressure gradient in the occluded region of the channel, and it declines near the boundaries.
- Trapping process is declined against the addition of SWCNTs volume fraction and Hall number, while it enhances against Hartmann number.

Fig. 28 Streamlines in case of SWCNTs and MWCNTs via $m = 0.5, m = 1.0, m = 1.5$

Fig. 29 Streamlines in case of SWCNTs and MWCNTs via $M = 1.5, M = 2.0, M = 3.0$
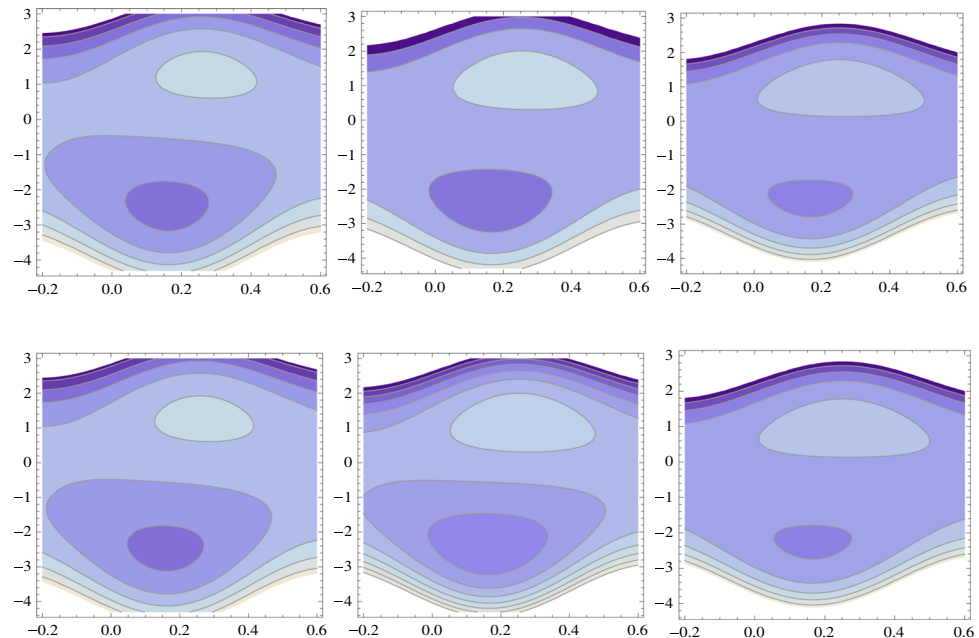
- The velocity enhances near the center of the channel against inclination angle, Hall number and inclination angle of magnetic field, and it decreases against Hartmann number and Froude number.

- Pressure gradient decreases for larger Froude number, Hall number and inclination angle of magnetic field, and it shows increasing behavior for larger volume fraction at the center of the channel.

- Inclination angle, Brinkman number, Dufour number, Froude number, Hall number and inclination angle of magnetic field correspond to an increase in the temper-

ature, while it decreases against Hartmann number and Biot number.

- Concentration profile declines for larger Schmidt number and Soret number.

- Velocity and concentration profiles are noted higher by the addition of SWCNTs when compared to MWCNTs. The addition of MWCNTs in water corresponds to higher temperature than the addition of SWCNTs in water.

The findings of the current analysis have their possible utilization in biomedical engineering, namely diagnosis and treatment of diseases, magnetic drug delivery system (which
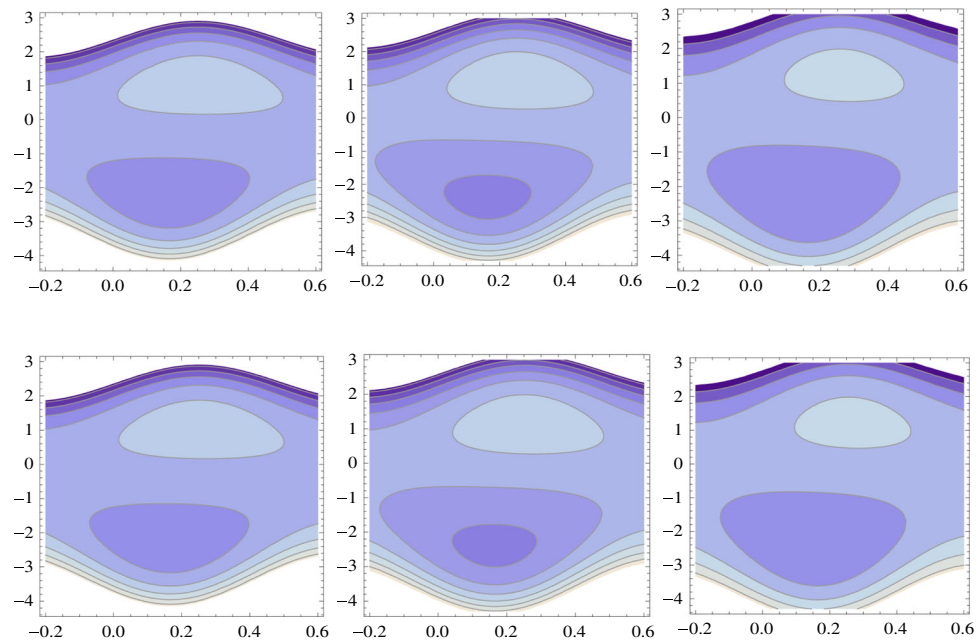
Fig. 30 Streamlines in case of SWCNTs and MWCNTs via $\alpha = \frac{\pi}{4}$, $\alpha = \frac{\pi}{3}$, $\alpha = \frac{\pi}{2}$
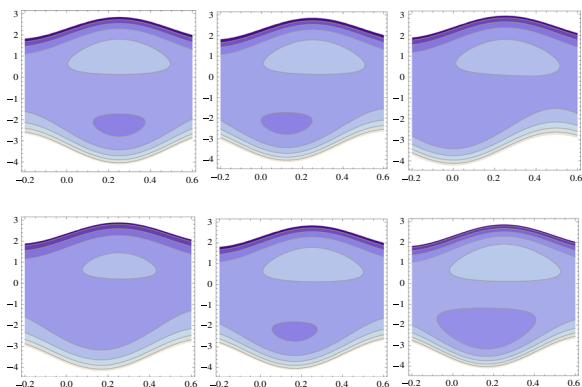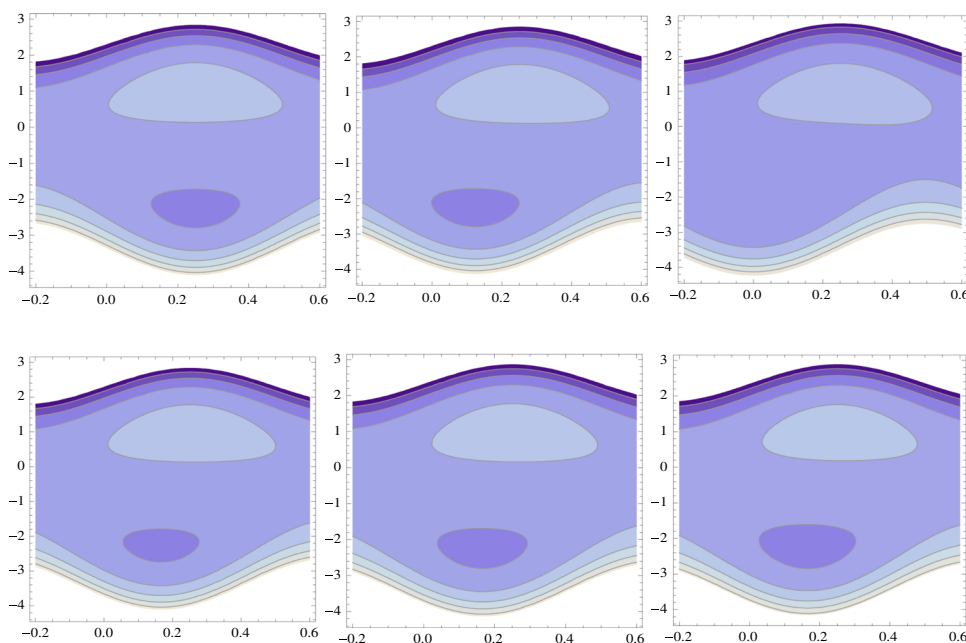

Fig. 31 Streamlines in case of SWCNTs and MWCNTs via $\phi_1 = 0.0$, $\phi_1 = \frac{\pi}{4}$, $\phi_1 = \frac{\pi}{2}$

$$\rho_{\text{nf}} \left(\frac{\partial}{\partial \bar{t}_\star} + \bar{U}_\star \frac{\partial}{\partial \bar{X}} + \bar{V}_\star \frac{\partial}{\partial \bar{Y}} \right) \bar{V}_\star = -\frac{\partial \bar{P}_\star}{\partial \bar{Y}} + \mu_{\text{nf}} \left(\frac{\partial^2 \bar{V}_\star}{\partial \bar{X}^2} + \frac{\partial^2 \bar{V}_\star}{\partial \bar{Y}^2} \right)$$
$$+ \frac{\sigma_{\text{nf}} B_0^2}{1+m^2} \sin\theta \left(\bar{U}_\star \cos\theta - \bar{V}_\star \sin\theta \right) - g\rho_{\text{nf}} \cos\alpha, \quad (14)$$

$$\rho_{\text{nf}} c_{\text{p}} \left(\frac{\partial}{\partial \bar{t}_\star} + \bar{U}_\star \frac{\partial}{\partial \bar{X}} + \bar{V}_\star \frac{\partial}{\partial \bar{Y}} \right) T_\star = \kappa_{\text{nf}} \left(\frac{\partial^2 T_\star}{\partial \bar{X}^2} + \frac{\partial^2 T_\star}{\partial \bar{Y}^2} \right)$$
$$+ \frac{\rho_{\text{nf}} D K_{\text{T}}}{c_s} \left(\frac{\partial^2 C_\star}{\partial \bar{X}^2} + \frac{\partial^2 C_\star}{\partial \bar{Y}^2} \right) + \mu_{\text{nf}} \left[2 \left(\frac{\partial \bar{U}_\star}{\partial \bar{X}} \right)^2 \right.$$
$$\left. + 2 \left(\frac{\partial \bar{V}_\star}{\partial \bar{Y}} \right)^2 + \left(\frac{\partial \bar{U}_\star}{\partial \bar{Y}} + \frac{\partial \bar{V}_\star}{\partial \bar{X}} \right)^2 \right], \quad (15)$$

$$\left(\frac{\partial}{\partial \bar{t}_\star} + \bar{U}_\star \frac{\partial}{\partial \bar{X}} + \bar{V}_\star \frac{\partial}{\partial \bar{Y}} \right) C_\star$$
$$= D \left(\frac{\partial^2 C_\star}{\partial \bar{X}^2} + \frac{\partial^2 C_\star}{\partial \bar{Y}^2} \right) + \frac{D K_{\text{T}}}{T_m} \left(\frac{\partial^2 T_\star}{\partial \bar{X}^2} + \frac{\partial^2 T_\star}{\partial \bar{Y}^2} \right). \quad (16)$$

The geometry of channel walls and boundary conditions are defined as

$$\bar{U}_\star = 0, \quad \kappa_{\text{nf}} \frac{\partial T_\star}{\partial \bar{Y}} = -\eta_1 (T_\star - T_{\text{a}}), \quad C_\star = C_0,$$

$$\text{at} \quad \bar{Y} = \bar{H}_1^\star(\bar{X}, \bar{t}) = a_1 \sin\left[\frac{2\pi}{\lambda} (\bar{X} - c\bar{t}) \right] + d_1^\star,$$

$$\bar{U}_\star = 0, \quad \kappa_{\text{nf}} \frac{\partial T_\star}{\partial \bar{Y}} = -\eta_2 (T_{\text{a}} - T_\star), \quad C_\star = C_1,$$

$$\text{at} \quad \bar{Y} = \bar{H}_2(\bar{X}, \bar{t}) = -a_2 \sin\left[\frac{2\pi}{\lambda} (\bar{X} - c\bar{t}) + \phi_1 \right] - d_2^\star. \quad (17)$$

Symmetric channel with waves out of phase ($\phi_1 = 0$) and waves in phase ($\phi_1 = \pi$), a_i and d_i^* ($i = 1, 2$) satisfies the

is used effectively as therapy for many life alarming diseases such as cancer), colloidal drug delivery systems (nanofluids are utilized to increase the efficiency of drug action) and in many other fields.

Appendix

The governing flow model under conversation laws is expressed as:

$$\frac{\partial \bar{V}_\star}{\partial \bar{Y}} + \frac{\partial \bar{U}_\star}{\partial \bar{X}} = 0, \quad (12)$$

$$\rho_{\text{nf}} \left(\frac{\partial}{\partial \bar{t}_\star} + \bar{U}_\star \frac{\partial}{\partial \bar{X}} + \bar{V}_\star \frac{\partial}{\partial \bar{Y}} \right) \bar{U}_\star = -\frac{\partial \bar{P}_\star}{\partial \bar{X}} + \mu_{\text{nf}} \left(\frac{\partial^2 \bar{U}_\star}{\partial \bar{X}^2} + \frac{\partial^2 \bar{U}_\star}{\partial \bar{Y}^2} \right)$$
$$- \frac{\sigma_{\text{nf}} B_0^2}{1+m^2} \cos\theta \left(\bar{U} \cos\theta - \bar{V}_\star \sin\theta \right) + g\rho_{\text{nf}} \sin\alpha, \quad (13)$$

condition:

$$a_1^2 + a_2^2 + 2a_1 a_2 \cos\phi \le (d_1^\star + d_2^\star)^2. \tag{18}$$

Letting

$$\left.\begin{array}{l} \bar{x} = \bar{X} - c\bar{t}_\star \quad \bar{y} = \bar{Y}, \quad \bar{u}_\star(\bar{x},\bar{y}) = \bar{U}_\star(\bar{X},\bar{Y},\bar{t}_\star) - c, \\ \bar{v}_\star(\bar{x},\bar{y}) = \bar{V}_\star(\bar{X},\bar{Y},\bar{t}_\star), \quad \bar{p}(\bar{x},\bar{y}) = \bar{P}_\star(\bar{X},\bar{Y},\bar{t}_\star). \end{array}\right\} \tag{19}$$

In wave frame $(\bar{x},\bar{y})$, the equations become

$$\frac{\partial \bar{u}_\star}{\partial \bar{x}} + \frac{\partial \bar{v}_\star}{\partial \bar{y}} = 0, \tag{20}$$

$$\rho_{\rm nf}\left(\bar{u}_\star \frac{\partial}{\partial \bar{x}} + \bar{v}_\star \frac{\partial}{\partial \bar{y}}\right)\bar{u}_\star = -\frac{\partial \bar{p}_\star}{\partial \bar{x}} + \mu_{\rm nf}\left(\frac{\partial^2 \bar{u}_\star}{\partial \bar{x}^2} + \frac{\partial^2 \bar{u}_\star}{\partial \bar{y}^2}\right)$$
$$- \frac{\sigma_{\rm nf} B_0^2}{1+m^2}\cos\theta\Big((\bar{u}_\star + c)\cos\theta - \bar{v}_\star \sin\theta\Big) + g\rho_{\rm nf}\sin\alpha, \tag{21}$$

$$\rho_{\rm nf}\left(\bar{u}_\star \frac{\partial}{\partial \bar{x}} + \bar{v}_\star \frac{\partial}{\partial \bar{y}}\right)\bar{v}_\star = -\frac{\partial \bar{p}_\star}{\partial \bar{y}} + \mu_{\rm nf}\left(\frac{\partial^2 \bar{v}_\star}{\partial \bar{x}^2} + \frac{\partial^2 \bar{v}_\star}{\partial \bar{y}^2}\right)$$
$$+ \frac{\sigma_{\rm nf} B_0^2}{1+m^2}\sin\theta\Big((\bar{u}_\star + c)\cos\theta - \bar{v}_\star \sin\theta\Big) - g\rho_{\rm nf}\cos\alpha, \tag{22}$$

$$\rho_{\rm nf} c_{\rm p}\left(\bar{u}_\star \frac{\partial}{\partial \bar{x}} + \bar{v}_\star \frac{\partial}{\partial \bar{y}}\right)T_\star = \kappa_{\rm nf}\left(\frac{\partial^2 T_\star}{\partial \bar{x}^2} + \frac{\partial^2 T_\star}{\partial \bar{y}^2}\right)$$
$$+ \mu_{\rm nf}\left(2\left(\frac{\partial \bar{u}_\star}{\partial \bar{x}}\right)^2 + 2\left(\frac{\partial \bar{v}_\star}{\partial \bar{y}}\right)^2 + \left(\frac{\partial \bar{u}_\star}{\partial \bar{y}} + \frac{\partial \bar{v}_\star}{\partial \bar{x}}\right)^2\right)$$
$$+ \frac{\rho_{\rm nf} D K_{\rm T}}{T_m}\left(\frac{\partial^2 C_\star}{\partial \bar{X}^2} + \frac{\partial^2 C_\star}{\partial \bar{Y}^2}\right), \tag{23}$$

$$\left(\bar{u}_\star \frac{\partial}{\partial \bar{x}} + \bar{v}_\star \frac{\partial}{\partial \bar{y}}\right)C_\star = D\left(\frac{\partial^2 C_\star}{\partial \bar{x}^2} + \frac{\partial^2 C_\star}{\partial \bar{y}^2}\right) + \frac{D K_{\rm T}}{T_m}\left(\frac{\partial^2 T_\star}{\partial \bar{x}^2} + \frac{\partial^2 T_\star}{\partial \bar{y}^2}\right). \tag{24}$$

Equation (20) is satisfied trivially, while Eqs. (21–24) using Eq. (11) become

$$\delta\mathrm{Re}\left(u_\star \frac{\partial}{\partial x} + v_\star \frac{\partial}{\partial y}\right)u_\star = -\frac{\partial p_\star}{\partial x} + \delta^2 \frac{\partial^2 u_\star}{\partial x^2} + \frac{\partial^2 u_\star}{\partial y^2}$$
$$- \frac{M^2}{1+m^2}\cos\theta\Big(u_\star \cos\theta - v_\star \delta \sin\theta + \cos\theta\Big) + \frac{Re\sin\alpha}{Fr}, \tag{25}$$

$$\delta^3\mathrm{Re}\left(u_\star \frac{\partial}{\partial x} + v_\star \frac{\partial}{\partial y}\right)v_\star = -\frac{\partial p_\star}{\partial y} + \delta^2\left(\delta^2 \frac{\partial^2 v_\star}{\partial x^2} + \frac{\partial^2 v_\star}{\partial y^2}\right)$$
$$+ \frac{M^2}{1+m^2}\delta\sin\theta\Big(u_\star \cos\theta - \delta v_\star \sin\theta + \cos\theta\Big) - \delta\frac{Re\cos\alpha}{Fr}, \tag{26}$$

$$\delta\mathrm{Pe}\left(u_\star \frac{\partial}{\partial x} + v_\star \frac{\partial}{\partial y}\right)\gamma = \delta^2 \frac{\partial^2 \gamma}{\partial x^2} + \frac{\partial^2 \gamma}{\partial y^2} + \mathrm{PrDu}\left(\delta^2 \frac{\partial^2 \varphi}{\partial x^2} + \frac{\partial^2 \varphi}{\partial y^2}\right)$$
$$+ \mathrm{Br}\left[2\delta^2\left(\frac{\partial u_\star}{\partial x}\right)^2 + 2\delta^2\left(\frac{\partial v_\star}{\partial y}\right)^2 + \left(\frac{\partial u_\star}{\partial y} + \delta^2 \frac{\partial v_\star}{\partial x}\right)^2\right], \tag{27}$$

$$\delta\mathrm{Re}\left(u_\star \frac{\partial}{\partial x} + v_\star \frac{\partial}{\partial y}\right)\varphi = \frac{1}{\mathrm{Sc}}\left(\delta^2 \frac{\partial^2 \varphi}{\partial x^2} + \frac{\partial^2 \varphi}{\partial y^2}\right) + \mathrm{Sr}\left(\delta^2 \frac{\partial^2 \gamma}{\partial x^2} + \frac{\partial^2 \gamma}{\partial y^2}\right). \tag{28}$$

References

1. Nisar, Z.; Hayat, T.; Alsaedi, A.; Ahmad, B.: Significance of activation energy in radiative peristaltic transport of Eyring–Powell nanofluid. Int. Commun. Heat Mass Transf. **116**, 104655 (2020)
2. Hayat, T.; Muhammad, T.; Shehzad, S.A.; Alsaedi, A.: Three dimensional rotating flow of Maxwell nanofluid. J. Mol. Liq. **229**, 495–500 (2017)
3. Babazadeh, H.; Muhammad, T.; Shakeriaski, F.; Ramzan, M.; Hajizadeh, M.R.: Nanomaterial between two plates which are squeezed with impose magnetic force. J. Therm. Anal. Calorim. (2020). https://doi.org/10.1007/s10973-019-08706-7
4. Hayat, T.; Muhammad, T.; Shehzad, S.A.; Alsaedi, A.: Modeling and analysis for hydromagnetic three-dimensional flow of second grade nanofluid. J. Mol. Liq. **221**, 93–101 (2016)
5. Sheikholeslami, M.; Hayat, T.; Alsaedi, A.: Numerical study for external magnetic source influence on water based nanofluid convective heat transfer. Int. J. Heat Mass Trans. **106**, 745–755 (2017)
6. Ellahi, R.: The effects of MHD and temperature dependent viscosity on the flow of non-Newtonian nanofluid in a pipe: analytical solutions. Appl. Math. Model. **37**, 1451–1467 (2013)
7. Riaz, A.; Khan, S.D.; Zeeshan, A.; Khan, S.U.; Hassan, M.; Muhammad, T.: Thermal analysis of peristaltic flow of nanosized particles within a curved channel with second-order partial slip and porous medium. J. Therm. Anal. Calorim. **2020**, 1–13 (2020)
8. Hayat, T.; Hussain, Z.; Muhammad, T.; Alsaedi, A.: Effects of homogeneous and heterogeneous reactions in flow of nanofluids over a nonlinear stretching surface with variable surface thickness. J. Mol. Liq. **221**, 1121–1127 (2016)
9. Nisar, Z.; Hayat, T.; Alsaedi, A.; Ahmad, B.: Wall properties and convective conditions in MHD radiative peristalsis flow of Eyring–Powell nanofluid. J. Therm. Anal. Calorim. (2020). https://doi.org/10.1007/s10973-020-09576-0
10. Awais, M.; Shah, Z.; Parveen, N.; Ali, A.; Kumam, P.; Thounthong, P.: MHD effects on ciliary-induced peristaltic flow coatings with rheological hybrid nanofluid. Coatings **10**, 186 (2020)
11. Bhatti, M.M.; Riaz, A.; Zhang, L.; Sait, S.M.; Ellahi, R.: Biologically inspired thermal transport on the rheology of Williamson hydromagnetic nanofluid flow with convection: an entropy analysis. J. Therm. Anal. Calorim. **2020**, 1–16 (2020)
12. Bhatti, M.M.; Marin, M.; Zeeshan, A.; Ellahi, R.; Abdelsalam, S.I.: Swimming of motile gyrotactic microorganisms and nanoparticles in blood flow through anisotropically tapered arteries. Front. Phys. **8**, 95 (2020)
13. Bhatti, M.M.; Ellahi, R.; Zeeshan, A.; Marin, M.; Ijaz, N.: Numerical study of heat transfer and Hall current impact on peristaltic propulsion of particle-fluid suspension with compliant wall properties. Modern Phys. Lett. B **35**, 1950439 (2019)
14. Shapiro, A.H.: Pumping and retrograde diffusion in peristaltic waves. In: Proceedings of the Workshop on Ureteral Reflux in Children, pp. 109–126. Nat. Acad. Sci., Washington, DC (1967)
15. Latham, T.W.: Fluid motion in a peristaltic pump. M.S. Thesis. MIT, Cambridge (1966)
16. Hayat, T.; Ahmed, B.; Abbasi, F.M.; Alsaedi, A.: Hydromagnetic peristalsis of water based nanofluids with temperature dependent viscosity: a comparative study. J. Mol. Liq. **234**, 324–329 (2017)
17. Nadeem, S.; Maraj, E.N.: The mathematical analysis for peristaltic flow of hyperbolic tangent fluid in a curved channel. Commun. Theor. Phys. **59**, 729–736 (2013)
18. Sucharitha, G.; Lakshminarayana, P.; Sandeep, N.: Joule heating and wall flexibility effects on the peristaltic flow of magnetohydrodynamic nanofluid. Int. J. Mech. Sci. **132**, 52–62 (2017)
19. Hayat, T.; Aslam, N.; Alsaedi, A.; Rafiq, M.: Numerical study for MHD peristaltic transport of Sisko nanofluid in a curved channel. Int. J. Heat Mass Trans. **109**, 1281–1288 (2017)

20. Bhatti, M.M.; Zeeshan, A.; Ellahi, R.: Simultaneous effects of coagulation and variable magnetic field on peristaltically induced motion of Jeffrey nanofluid containing gyrotactic microorganism. Microvasc. Res. **110**, 32–42 (2017)

21. Hayat, T.; Saleem, A.; Tanveer, A.; Alsaadi, F.: Numerical study for MHD peristaltic flow of Williamson nanofluid in an endoscope with partial slip and wall properties. Int. J. Heat Mass Trans. **114**, 1181–1187 (2017)

22. Abbasi, F.M.; Hayat, T.; Ahmad, B.: Peristaltic transport of copper–water nanofluid saturating porous medium. Physica E **67**, 47–53 (2015)

23. Tripathi, D.; Bég, O.A.: A study on peristaltic flow of nanofluids: application in drug delivery systems. Int. J. Heat Mass Trans. **70**, 61–70 (2014)

24. Hayat, T.; Tanveer, A.; Alsaedi, A.: Numerical analysis of partial slip on peristalsis of MHD Jeffery nanofluid in curved channel with porous space. J. Mol. Liq. **224**, 944–953 (2016)

25. Kothandapani, M.; Prakash, J.; Pushparaj, V.: Effects of thermal radiation parameter and magnetic field on the peristaltic motion of Williamson nanofluids in a tapered asymmetric channel. Int. J. Heat Mass Trans. **81**, 234–245 (2015)

26. Kothandapani, M.; Prakash, J.: Effect of radiation and magnetic field on peristaltic transport of nanofluids through a porous space in a tapered asymmetric channel. J. Magn. Magn. Mater. **378**, 152–163 (2015)

27. Hayat, T.; Iqbal, R.; Tanveer, A.; Alsaedi, A.: Mixed convective peristaltic transport of Carreau–Yasuda nanofluid in a tapered asymmetric channel. J. Mol. Liq. **223**, 1100–1113 (2016)

28. Reddy, M.G.; Makinde, O.D.: Magnetohydrodynamic peristaltic transport of Jeffrey nanofluid in an asymmetric channel. J. Mol. Liq. **223**, 1242–1248 (2016)

29. Ellahi, R.; Hussain, F.; Abbas, S.A.; Sarafraz, M.M.; Goodarzi, M.; Shadloo, M.S.: Study of two-phase Newtonian nanofluid flow hybrid with hafnium particles under the effects of slip. Inventions **5**, 6 (2020)

30. Prakash, J.; Sharma, A.; Tripathi, D.: Thermal radiation effects on electroosmosis modulated peristaltic transport of ionic nanoliquids in biomicrofluidics channel. J. Mol. Liq. **249**, 843–855 (2018)

31. Hayat, T.; Akram, J.; Alsaedi, A.; Zahir, H.: Endoscopy effect in mixed convective peristalsis of Powell–Eyring nanofluid. J. Mol. Liq. **254**, 47–54 (2018)

32. Tripathi, D.; Sharma, A.; Bég, O.A.: Joule heating and buoyancy effects in electroosmotic peristaltic transport of aqueous nanofluids through a microchannel with complex wave propagation. Adv. Powder Technol. **29**, 639–653 (2018)

33. Hayat, T.; Shafique, M.; Tanveer, A.; Alsaedi, A.: Hall and ion slip effects on peristaltic flow of Jeffrey nanofluid with Joule heating. J. Magn. Magn. Mater. **407**, 51–59 (2016)

34. Ellahi, R.; Bhatti, M.M.; Pop, I.: Effects of Hall and ion slip on MHD peristaltic flow of Jeffrey fluid in a non-uniform rectangular duct. Int. J. Numer. Methods Heat Fluid Flow **26**, 1802–1820 (2016)

35. Gaffar, S.A.; Prasad, V.R.; Reddy, E.K.: MHD free convection flow of Eyring–Powell fluid from vertical surface in porous media with Hall/ionslip currents and ohmic dissipation. Alex. Eng. J. **55**, 875–905 (2016)

36. Ahmed, B.; Hayat, T.; Alsaedi, A.; Abbasi, F.M.: Entropy generation analysis for peristaltic motion of Carreau–Yasuda nanomaterial. Phys. Scr. **95**, 055804 (2020)

37. Asha, S.K.; Sunitha, G.: Thermal radiation and Hall effects on peristaltic blood flow with double diffusion in the presence of nanoparticles. Case Stud. Therm. Eng. **17**, 100560 (2020)

38. Hayat, T.; Rafiq, M.; Alsaedi, A.: Investigation of Hall current and slip conditions on peristaltic transport of Cu–water nanofluid in a rotating medium. Int. J. Therm. Sci. **112**, 129–141 (2017)

39. Noreen, S.; Qasim, M.: Influence of Hall current and viscous dissipation on pressure driven flow of pseudoplastic fluid with heat generation: a mathematical study. PLoS ONE **10**, e0129588 (2015)

40. Bhatti, M.M.; Abbas, M.A.; Rashidi, M.M.: Effect of Hall and ion slip on peristaltic blood flow of Eyring–Powell fluid in a non-uniform porous channel. World J. Model. Simul. **12**, 268–279 (2016)

41. Nirmala, K.; Muthuraj, R.; Srinivas, S.; Lourdu, D.: Immaculate, combined effects of hall current, wall slip, viscous dissipation and Soret effect on MHD Jeffrey fluid flow in a vertical channel with peristalsis. J. Heat Mass Trans. **12**, 131–165 (2015)

42. Srinivas, S.; Kothandapani, M.: The influence of heat and mass transfer on MHD peristaltic flow through a porous space with compliant walls. Appl. Math. Comput. **213**, 197–208 (2009)

43. Saleem, M.; Haider, A.: Heat and mass transfer on peristaltic transport of non-Newtonian fluid with creeping flow. Int. J. Heat Mass Trans. **68**, 514–526 (2014)

44. Hayat, T.O.; Rafiq, M.; Alsaadi, F.; Ayub, M.: Soret and Dufour effects on peristaltic transport in curved channel with radial magnetic field and convective conditions. J. Magn. Magn. Mater **405**, 358–369 (2016)

45. Hayat, T.; Yasmin, H.; Al-Yami, M.: Soret and Dufour effects in peristaltic transport of physiological fluids with chemical reaction: a mathematical analysis. Comput. Fluids **89**, 242–253 (2015)

46. Hayat, T.; Iqbal, R.; Tanveer, A.; Alsaedi, A.: Soret and Dufour effects in MHD peristalsis of pseudoplastic nanofluid with chemical reaction. J. Mol. Liq. **220**, 693–706 (2016)

47. Hayat, T.; Farooq, S.; Alsaedi, A.; Ahmad, B.: Numerical study for Soret and Dufour effects on mixed convective peristalsis of Oldroyd 8-constants fluid. Int. J. Therm. Sci. **112**, 68–81 (2017)

48. Khan, S.A.; Hayat, T.; Khan, M.I.; Alsaedi, A.: Salient features of Dufour and Soret effect in radiative MHD flow of viscous fluid by a rotating cone with entropy generation. Int. J. Hydrog. Energy (2020). https://doi.org/10.1016/j.ijhydene.2020.03.123

49. Alolaiyan, H.; Riaz, A.; Razaq, A.; Saleem, N.; Zeeshan, A.; Bhatti, M.M.: Effects of double diffusion convection on third grade nanofluid through a curved compliant peristaltic channel. Coatings **10**, 154 (2020)

50. Hina, S.; Mustafa, M.; Hayat, T.; Alotaibi, N.D.: On peristaltic motion of pseudoplastic fluid in a curved channel with heat/mass transfer and wall properties. Appl. Math. Comput. **263**, 378–391 (2015)

51. Bhatti, M.M.; Zeeshan, A.; Ellahi, R.; Ijaz, N.: Heat and mass transfer of two phase flow with Electric double layer effects induced due to peristaltic propulsion in the presence of transverse magnetic field. J. Mol. Liq. **230**, 237–246 (2017)

52. Xue, Q.: Model for thermal conductivity of carbon nanotube based composites. Phys. B Condens. Matter **368**, 302–307 (2005)

53. Khan, W.A.; Khan, Z.H.; Rahi, R.: Fluid flow and heat transfer of carbon nanotubes along a plate with Navier slip boundary. Appl. Nanosci. **4**, 633–41 (2014)